Materials Chemistry and Physics 230 (2019) 83–92

Contents lists available at ScienceDirect

Materials Chemistry and Physics

journal homepage: www.elsevier.com/locate/matchemphys

Multi-scale mapping for collagen-regulated mineralization in bone remodeling of additive manufacturing porous implants

Pei-I. Tsai[a,b], Tu-Ngoc Lam[a], Meng-Huang Wu[c,d], Kuan-Ying Tseng[a], Yuan-Wei Chang[a], Jui-Sheng Sun[e], Yen-Yao Li[f,g], Ming-Hsueh Lee[h], San-Yuan Chen[a], Chung-Kai Chang[a,i], Chun-Jen Su[i], Chia-Hsien Lin[i], Ching-Yu Chiang[i], Ching-Shun Ku[i], Nien-Ti Tsou[a], Shao-Ju Shih[j], Chun-Chieh Wang[i,**], E-Wen Huang[a,*]

[a] Department of Materials Science and Engineering, National Chiao Tung University, 1001 University Road, Hsinchu, 30010, Taiwan, ROC
[b] Biomedical Technology and Device Research Laboratories, Industrial Technology Research Institute, Chutung, Hsinchu County, Taiwan, ROC
[c] Department of Orthopaedics, Taipei Medical University Hospital, No. 252, Wuxing St, Xinyi District, Taipei, 11031, Taiwan, ROC
[d] Department of Orthopedics, College of Medicine, Taipei Medical University, No. 250, Wuxing St, Xinyi District, Taipei, 11031, Taiwan, ROC
[e] Department of Orthopedic Surgery, National Taiwan University Hospital, No. 7, Chung-Shan South Road, Taipei, 10002, Taiwan, ROC
[f] Department of Orthopedic Surgery, Chang Gung Memorial Hospital, No. 6, Sec. W., Jiapu Rd., Puzi City, Chiayi County, 613, Taiwan, ROC
[g] College of Medicine, Chang Gung University, No. 259, Wenhua 1st Rd., Guishan Dist., Taoyuan, 33302, Taiwan, ROC
[h] Department of Neurosurgery, Chang Gung Memorial Hospital, No. 6, Sec. W., Jiapu Rd., Puzi City, Chiayi County, 613, Taiwan, ROC
[i] National Synchrotron Radiation Research Center, Hsinchu, 30076, Taiwan, ROC
[j] Department of Materials Science and Engineering, National Taiwan University of Science and Technology, No. 43, Sec. 4, Keelung Road, Taipei 10607, Taiwan, ROC

HIGHLIGHTS

- The pig implanted with 3D printed Ti−6Al−4V has greater bone growth.
- Ti−6Al−4V hastens surface osseointegration much better than commercial Ti and Ta.
- The mature bone in Ti−6Al−4V indicates higher crystallinity of hydroxyapatite.
- Our findings suggest key signs in determining how the healthy normal bone grows.

ARTICLE INFO

Keywords:
Implant
Additive manufacturing
X-ray tomography
Small X-ray angle scattering
Nano X-ray Laue diffraction mapping

ABSTRACT

Long term success of metallic fusion cages depends on mechanobiological processes through the bone incorporation and rich osseointegration. An optimal configuration of porous titanium-aluminum-vanadium (Ti−6Al−4V) implant fabricated via the additive manufacturing was evaluated in complimentary structure examinations to investigate the growth of autologous osseous at multi-length scales. X-ray microcomputed tomography (micro-CT) and transmission X-ray microscopy (TXM) using newly-built analysis method indicate the porous Ti−6Al−4V is much better for bone ingrowth compared to commercially non-porous titanium (Ti) and porous tantalum (Ta) implants at the ultramicrostructural level. The evolution of bone formation and remodeling acquired by nano X-ray Laue diffraction mapping exhibits the isotropic orientation and low crystallinity of all newly formed bone whereas mature bone in Ti−6Al−4V discloses the preferential alignment and higher crystallinity volumes of constituent hydroxyapatite (HA) crystallites. The high degree in mineral crystallinity of the fully mature bone suggests additive manufactured Ti−6Al−4V pores enhance the collagen-regulated mineralization.

1. Introduction

The prevalence of osteoporosis seriously influences both men and women, especially for the seniors. More specifically, the patients with osteoporosis face higher risks of disability, hospitalization, and even mortality; hence, osteoporosis therapy is gaining more and more

* Corresponding author. Department of Materials Science and Engineering, National Chiao Tung University, 1001 University Road, Hsinchu, 30010, Taiwan, ROC.
** Corresponding author.
E-mail addresses: wang.jay@nsrrc.org.tw (C.-C. Wang), EwenHUANG@nctu.edu.tw (E.-W. Huang).

https://doi.org/10.1016/j.matchemphys.2019.03.047
Received 3 September 2018; Received in revised form 13 March 2019; Accepted 15 March 2019
Available online 19 March 2019
0254-0584/ © 2019 The Authors. Published by Elsevier B.V. This is an open access article under the CC BY-NC-ND license (http://creativecommons.org/licenses/BY-NC-ND/4.0/).

attention for the on-going aging society [1]. With population aging, osteoporosis and fracture eventually become the growing burden of not only the patients but also their families. The fracture in bone has been proposed as the major reason of falls which often occurs in the elderly population [2]. As a result, a great need of implants for the bone healing is rising. Although there are various models describing the bone fracture and strength, more and more research is requisite to elucidate how the shape and strength of bones may originate from the interplay of mechanical, biological, and structural process regulated by the constituent periosteal osteoblasts [3].

The structure of bone tissue, a hierarchical nano-composite organization, originates from an intrinsically intricate process in which collagenous extracellular matrix (ECM) secreted by osteoblasts cells and evolves through mineralization of HA mineral crystals in a microscopic viewpoint [4]. Osteoblasts cells are mainly responsible for collagen matrix synthesis that regulates the subsequently mineral nucleation and growth of low crystalline HA particles. New bone is produced through ossification by osteoblasts cells before occurring sequent organized mineralization [5]. The degree of mineralization as well as the size, shape, or orientation of the HA mineral crystals in type I collagen fibers are possibly changeable [6]. In the type I collagen fibril, the distinct collagen molecules arrange in a staggered order forming periodic gaps or spaces along the fibril in which the mineral crystals are not only trapped but also maturely grown [6,7]. The matrix of mature bone has a lamellar structure created by parallel or concentric layers of the type I collagen fibrils [5]. The mineralization of HA crystallites is strongly affected by the architecture, structure, and porosity of the scaffolds [8]. Furthermore, the mineralization of the implants with the appropriate orientation of the ECM regulating HA crystallites also plays a critical role [7].

The assistant of interbody spinal fusion devices in spinal fusion bone healing and autologous bone graft incorporation is one of the widespread and rapidly developed research fields in recent years. Such spinal fusion cages are requiring several primary types of benchmarking for their widely potential applications in spinal arthrodesis surgery [9]. An excellent fixation is expected for initial mechanical stability in inhibiting displacements so that implants can hold by themselves in living body. Another important criteria is to allow the autologous bone ingrowth inside the cage under large mechanical forces as well as to promote a good attachment between living host bone and surface of implant, which is named osseointegration [10]. Providing sufficient strength to restrain significant bone resorption secondary to stress shielding effects caused by the stiffness mismatch between the surrounding bone and the implant is a strong need for the enhancement of long term motion segmental stability [9]. To satisfy the vital requirements for spinal fusion implants, recent efforts have focused on different cage architecture designs [11–14] while numerous research has made a great attempt to various biomechanical implants in vivo studies [9,12,15–17].

Most of spinal fusion cages are designed with cylindrical or various complex shapes at the outer shells and hollow in the center which autologous bone apposition can be filled in. The graft hole within the cage is expected to enable an entire osseous ingrowth and bone graft incorporation in accelerating the bone fusion. Metallic implants have been widely applied in the manufacture of spinal fixation devices since they possess outstanding characteristics such as biocompatibility and resistance to corrosion, which are extremely appropriate to high load bearing applications. However, some of them are too strong to match bone elastic properties that lead to unexpected stress shielding and thus the unsuccessful of the implants. Among commonly used materials, Ti and Ti alloys have been well known as typically preferable implants with respect to theirs sufficient strength and light weight, as well an obviously successful osseous appositional [18–20]. In addition, Ti implants provide better visualization of magnetic resonance imaging (MRI) without serious interference of metal artifacts that is a main issue of firstly successfully used stainless steel implants. It is noted that high-quality imaging characteristics conducted by radiographic, MRI, or micro-CT play critical roles in evaluating the biocompatibility of implanted materials and the evolution of surrounding bone tissue in direct anchorage to the implants, postoperatively.

Many efforts during the past two decades have been made to fabricate the porous and rough-surfaced implants rather than the non-porous and smooth-surfaced structures since a great number of in vitro and in vivo studies has disclosed convincing evidence in better biomechanical attachment, strong bone tissue-metal interface contact [21,22] and effective reduction of bone loss secondary to stress shielding by 75% induced by porous metallic or alloy [23]. Designing the architecture of the porous implants with a high degree of interconnected porosity and good adaptability to surrounding bone tissue have relentlessly urged the development of advanced manufacturing techniques that require a highly precise control, reliability, reproducibility, and cost-effectiveness [24–26]. With the rapid progress in additive manufacturing, three-dimensional (3D) printing of Ti and Ti alloys enable the construction of diverse implant geometries with well-controllable pore networks and high degree of customization. The most prevalent Ti alloy, 3D printed Ti−6Al−4V, has recently emerged as a potential candidate for spine fusion implants due to not only its superior microstructural and biomechanical performances [27,28] but also its promotion in bone formation and osseointegration, as reported by several in-vivo studies [29–31]. Currently, commercial Ta metal with a high porosity of 80% is the most popular fusion cage found in the market. Besides being known to produce less image distortion than Ti does [32], porous Ta also owns better mechanical properties, good endurance, high ductility, greater bone growth [33,34]. However, there have been very few studies focused on the nanostructural characterization of the constituent HA crystallites in bone tissue formed surrounding the implants. It is noted that bone is a complicated hierarchical organization which comprises an orderly arrangement of structural components from macrostructure to subnanostructural scale [35]. Clarifying the anisotropy orientation and crystallographic nanostructure of HA originated from the mineralized bone formed around the implants is crucial to determine the quality of bone ingrowth around the fusion cages.

In the current study, the porous Ti−6Al−4V cage produced by the selective laser melting (SLM) process, a rapid prototyping process, provides highly interconnected pore network structure with a high volume porosity of 60% and the optimal pore size below 500 μm for better bone growth [36–38]. SLM technique employs a high power-density laser to melt and fuse successive layers of metallic powders and thus produces metal scaffolds with diverse designs via the assistance of computer aided design (CAD) software [39]. With the use of SLM process, tuning a series of its controllable parameters is able to print 3D metal scaffolds with elaborate architectures and outstanding mechanical properties by tailoring pore shape, pore size, and volume of porosity [9,39–44]. The objective of this study is to investigate the host bone remodeled response to an interconnected pore Ti−6Al−4V alloy fabricated via 3D printing over commercially non-porous Ti alloy and porous Ta metal implants used in interbody spinal fusion cages in a pig model. The microstructural and ultramicrostructural evolution of bone regeneration as well as osseointegration zone between living bone and three different implants were assessed by the extent of various imaging modalities such as fluorescence, histological staining, micro-CT, and TXM analyses. The preferential crystal alignment of mineralized bone at nanometer scale was performed by synchrotron small angle X-ray scattering (SAXS). In addition, synchrotron X-ray diffraction (XRD) and nano X-ray Laue diffraction mapping was conducted to characterize the crystallographic structural properties of HA in newly formed bone and mature bone.

2. Materials and methods

2.1. Bone sample preparation

The three hollow-rectangular cages with the identical sizes of 11 mm in length, 14 mm in width, and 5 mm in height composed of commercially non-porous Ti, porous Ta (Zimmer, Parallel TM-S Fusion Device), and optimal porous Ti−6Al−4V were entirely filled with autologous bone and surgically embedded in the iliac bones which did not adopt to in vivo stress during daily activities of a healthy pig. Tetracycline was injected subcutaneously into the jugular vein of the pig three days before its scarification for subsequent observations of fluorescence images. The pig was sacrificed at settled time period of 6 months following surgery to ensure bone healing and complete bone graft incorporation. The study was performed strictly according to the regulations and laws of the Institutional Animal Care and Use Committee (IACUC) of Chang Gung Memorial Hospital in Chiayi, Taiwan. All animal experimental procedures were approved by the IACUC of Chang Gung Memorial Hospital (IACUC number: 2013121916). The bone sections were fixed in 10% formalin, then dehydrated in the gradient of alcohol, and finally embedded in polymethylmethacrylate (PMMA) to polymerize the specimens. The cross-section of each bone section with a certain thickness of 200 μm was carefully sliced perpendicularly to the longitudinal axis of the bone by using a diamond knife, which included particular regions of interest, namely, autologous bone, implant, and especially surrounding bone around the implants. To serve for better visualization in optical imaging, the bone specimens were polished by grinding system. Depending on specific analyses, further treatments of bone sections were accordingly processed.

2.2. Histological staining

Histological staining is indispensable for understanding the process of surrounding bone formation and remodeling around osteointegrated implants in vivo assessment. We herein particularly utilized RBS technique for the staining of ground section histology to distinguish the mineralized mature bone [45]. Microscopic observations of mature bone were appeared in pink color while those of metallic implants were presented in black color under a transmitted light microscopy via using the RBS staining. We followed the RBS staining protocol reported by Dorn & Hart Microedge. The RBS was heated to 55°-60°, followed by the staining process of bone specimens for 30 s to 2 min. The redundant stain was expelled by firstly rinsing the bone sections in water and then wiping them. Three different bone sections were withdrawn from the mixture of counterstain with acidified acid fuchsin and finally were dehydrated.

2.3. Fluorescence analysis

Fluorescence, in company with histological staining, has traditionally been considered as the standard technique to examine the degree of bone response at the bone-implant contact, thus yields to the valuation towards the success rate of fusion implants. In this work, tetracycline was used as fluorochrome for the fluorescence characteristics [46]. Fluorescence microscopy images were captured under the excitation wavelength of 467 nm and emission wavelength of 550 nm with the use of a specific wavelength of the green filter (ET405/40×). Slightly different brightness levels were detected in tetracycline-based analysis in which green fluorescence can appear to be brighter in the surface areas of newly formed bone.

2.4. Synchrotron X-ray microcomputed tomography

X-ray microcomputed tomography, a non-destructive technique, images the microstructures of living organs with a spatial resolution limitation of few micrometer scale. In the present study, we exploited synchrotron-based high-resolution X-ray micro-CT with a much higher spatial resolution within one micron compared to conventional in-house X-ray micro-CT, which was conducted at beamline BL01A1 at the National Synchrotron Radiation Research Center (NSRRC) in Taiwan. High-resolution X-ray micro-CT has specially attracted increasing attention in numerous research reports of bone microarchitecture and mineralization level in bone remodeling due to an evident contrast between bone and soft tissue. A feasible differentiation between new bone and mature bone around the implants was determined through a clear image contrast of grey scale color that reflects the absorption coefficient difference between new and mature bones of illuminated hard X-rays.

2.5. Synchrotron transmission X-ray microscopy

Transmission x-ray microscopy is also a non-destructive image microscopy technique, which enables the characterization of not only high-resolution X-ray radiography in two dimensions (2D) but also the internal microstructure tomography in three-dimensions (3D) [47,48]. With the aid of Fresnel-zone-plate and high flux synchrotron hard X-ray source at the wavelength of 1.54 Å (8 keV) at BL 01B1 beamline of NSRRC, the TXM can achieve a spatial resolution about 60 nm. The direct contacts of new bone, mature bone, and void areas were evidently distinguished with the naked eyes through sharp contrasts of 2D TXM images in grey scale color with such high spatial resolution.

2.6. Synchrotron small wide angle X-ray scattering

SAXS techniques have been extensively carried out to identify the structural characterizations in terms of the predominant orientation distribution, degree of crystalline arrangement, as well the shape and size of mineralized HA within the regenerating bone tissues at the nanometer scale structures [49]. The non-destructive SAXS techniques were implemented with the wavelength of 1.24 Å (10 keV) at BL23A1, NSRRC. The scattering patterns were collected from a 2D detector and calibrated by subtracting the background spectrum without the sample. The reconstructed images can be mapped at the identical regions of interest in bone specimens.

2.7. Synchrotron x-ray diffraction

Structural modifications of the mineral crystallites composed of HA at the molecular scale were examined by synchrotron radiation x-ray diffraction [35,50]. The same positions of new bone and mature bone surrounding the implants in bone sections observed by traditional analysis methods as well as X-ray micro-CT imaging were irradiated by X-ray radiation with the wavelength of 0.827 Å (15 keV) at BL01C2, NSRRC. Diffraction patterns obtained from the 2D detector were integrated into one dimension. The characterization in crystallographic textures of mineral crystallites acquired by XRD is capable of evaluating the progress of bone remodeling and bone mineralization during bone healing process in vivo experiments of three different implants.

2.8. Nano X-ray Laue diffraction

The scanning X-ray Laue diffraction method provided high spatial resolution to determine the crystal information in tiny regions of matters without any physical rotations compared to traditional X-ray method. This unique technique coupled with SEM for sample navigation and positioning enable fast mapping the distribution of inhomogeneous specimens. A pre-shaped Kirkpatrick-Baez mirror pair was utilized to focus polychromatic X-ray with energy covered from 5,000 to 30,000 eV and provided a focused X-ray with beam size better than 90 nm × 90 nm in lateral at Taiwan Photon Source (TPS) BL21A in NSRRC. The porous Ti−6Al−4V implant was mounted on a special

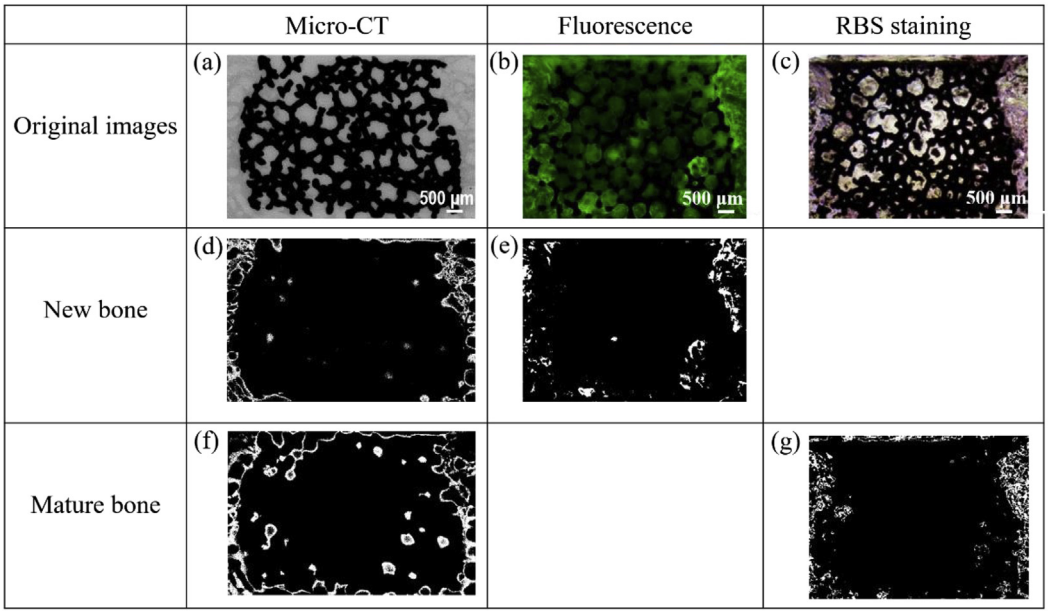

Fig. 1. Microscopic images of bone ingrowth around commercially porous Ta taken by (a) X-ray micro-CT, (b) fluorescence, and (c) RBS staining analyses at the same scale bar of 500 μm. The white areas of new bone (d) and mature bone (f) obtained by X-ray micro-CT. (e) The white regions of new bone observed by fluorescence. (g) The white zones of mature bone seen by RBS staining.

designed sample stage with 45° pre-tilted angle relative to the incident X-ray beam. A high sensitivity pixel array detector, in-vacuum PILATUS-6M, was employed to collect the Laue diffraction pattern. In this study, a 2D mapping with an area of 530 × 380 μm^2 covered by new bone and mature bone was scanned with a step size of 2.5 μm. Each mapping image comprises 212 × 152 pixels, and each pixel represents a Laue diffraction pattern. These patterns were analyzed by XMAS [51] software package to identify the crystal phase and crystallinity while the mapped images of total intensity, crystal orientation, and peak width were calculated and presented by our LabVIEW-based coding.

3. Results

3.1. New bone and mature bone observed by X-ray micro-CT

Fig. 1(a), (b), and (c) display the microscopic images obtained by X-ray micro-CT, fluorescence, and RBS staining of autologous bone around the commercially porous Ta implant at the same scale bar of 500 μm, respectively. The brighter zone of new bone in fluorescence and the stained pink area of mature bone in RBS staining can be clearly viewed with the naked eyes. In X-ray micro-CT image, the black and light-colored white regions represent the Ta metal implant and voids, respectively, while new bone and mature bone can be distinguished through the image contrast in grey scale color. No significant discrepancies were found for the presence of new born and mature bone by those imaging modalities. The white regions of new bone formation presented a good correlation between the micro-CT in Fig. 1 (d) and fluorescence images in Fig. 1 (e) while the white areas of mature bone expressed a good correspondence between the micro-CT images in Fig. 1 (f) and RBS staining in Fig. 1 (g). These results strongly affirm the potential role of micro-CT as a plausible and reliable technique for the characterization of bone regeneration.

3.2. Greater bone growth in uniform porous Ti−6Al−4V

The major differences in the evolution of bone remodeling around three distinct implants were examined by micro-CT. Fig. 2(a), (b), and (c) illustrate micro-CT images of surrounding bone around osteointegrated implants of Ti, Ti−6Al−4V, and Ta, respectively. Fig. 2(a), (d) and (g) exhibit negligible quantities of bone formation around the periphery of non-porous Ti implant and an extremely poor surface osseointegration between host bone and Ti cage. Micro-CT images of porous Ta and Ti−6Al−4V indicated that more osseous adaptation around these implants and more bone tissue growth into these porous surfaces rather than in the non-porous surface of Ti. Contrary to the commercially non-porous Ti, a well-designed architecture of Ti−6Al−4V implant in Fig. 2(b) with good interconnectivities of porous networks whose custom shapes, homogenous pore sizes, and distribution were uniform over the whole surface demonstrated promising capabilities of 3D printed alloy fabricated via SLM technique. Fig. 2(e) and (h) provide striking evidences in an entirely and perfectly uniform growth of the bone tissue not only around the periphery but also into the open interconnected pore networks of Ti−6Al−4V cage. Although the commercial Ta possessed a higher porosity volume up to 80%, the open micro-pore networks of irregular shapes and inhomogeneous pore sizes were randomly distributed and their interconnectivities were interrupted, as seen in Fig. 2(c). This leads to success of bone growth only around the periphery but into the open porous networks of Ta cage, as depicted in Fig. 2(f) and (i). The non-uniform bone formation in porous Ta may be attributed to the impact of inhomogeneous pore sizes on bone growth. It cannot be denied that 3D printed Ti−6Al−4V hastens the surface osseointegration much better than commercially non-porous Ti and porous Ta, despite the same living time of three implants in the pig.

3.3. Rich surface osseointegration in 3D printed Ti−6Al−4V

Besides being observed in microstructural regions by micro-CT, the evolution of surface osseointegration in ultramicrostructural levels can be evidently detected based on synchrotron-based transmission X-ray tomography with very high spatial resolution. Fig. 3(a), (b), and (c) display 2D TXM images of the interfacial contact between living host bone and surface of Ti, Ti−6Al−4V, and Ta implants, respectively. X-ray tomography provides ultramicrostructural details with very sharp contrasts in grey scale color which enables us to clearly distinguish the direct adherent of new bone, mature bone, and void regions with the naked eyes in Fig. 3(d), (g), and (j) for non-porous Ti; in Fig. 3(e), (h), and (k) for 3D printed porous Ti−6Al−4V; and in Fig. 3(f), (i), and (l)

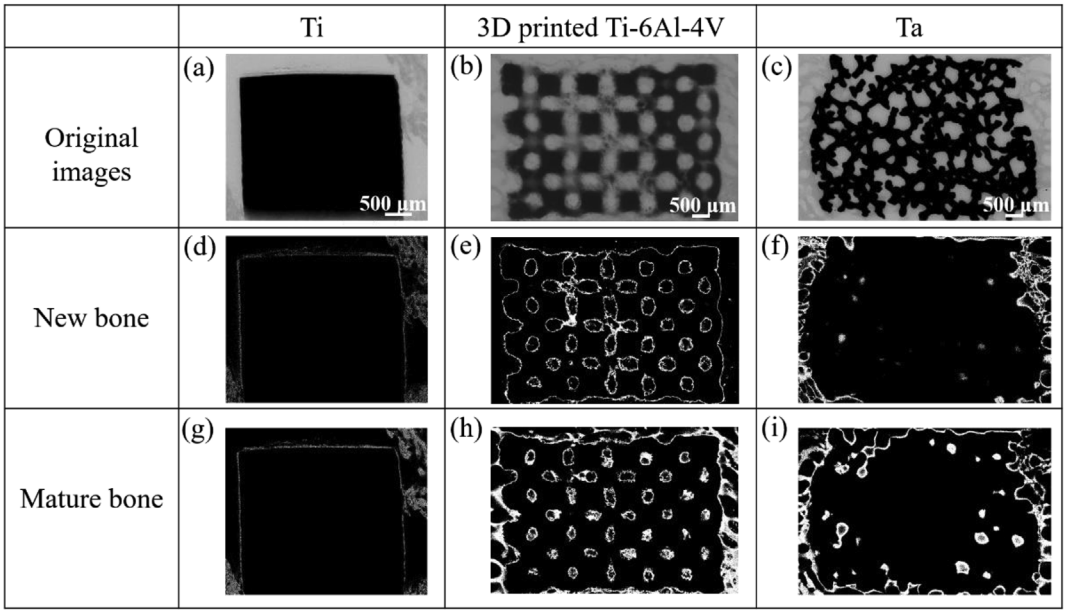

Fig. 2. X-ray micro-CT images of surrounding bone tissue growth around osteointegrated implants of (a) commercially non-porous Ti, (b) 3D printed porous Ti−6Al−4V, and (c) commercially porous Ta at the same scale bar of 500 μm. The white regions of new bone and mature bone of Ti were shown in (d) and (g), those of 3D printed Ti−6Al−4V in (e) and (h), and those of Ta in (f) and (i), respectively.

for porous Ta implants. The distribution of mature bone at the interfacial contact of non-porous Ti implant was uneven and discontinuous. The direct osseous apposition to non-porous Ti alloy did not easily occur, ascribed to restricted surface areas, which have no contribution to diminish the stress shielding effects, and this is one of the most serious obstacles of the non-porous structure-based implants in general. Contrary to the non-porous Ti, the growth region of mature bone was continuous in the porous Ti−6Al−4V and Ta implants. The most prominent feature was the large and continuous area of mature bone growth detected in 3D printed Ti−6Al−4V rather than in porous Ta implant. In short, the results of microstructural images infer a much impressive option of additive manufactured Ti−6Al−4V alloy in spinal fusion cage.

3.4. The most rapid bone ingrowth in 3D printed Ti−6Al−4V

From the perspective of bone incorporation, it is noteworthy to quantify the amount of new bone and mature bone surrounding three various implants, that was calculated in bone volume percentage to find out the most successful one in spinal fusion procedure. The surface area of bone ingrowth (bone volume) was determined as a ratio between the surface area of new bone or mature bone and the total areas of bone ingrowth, implant, and voids. Fig. 4 presents volume percentages of new bone and mature bone in commercially non-porous Ti, porous Ta,

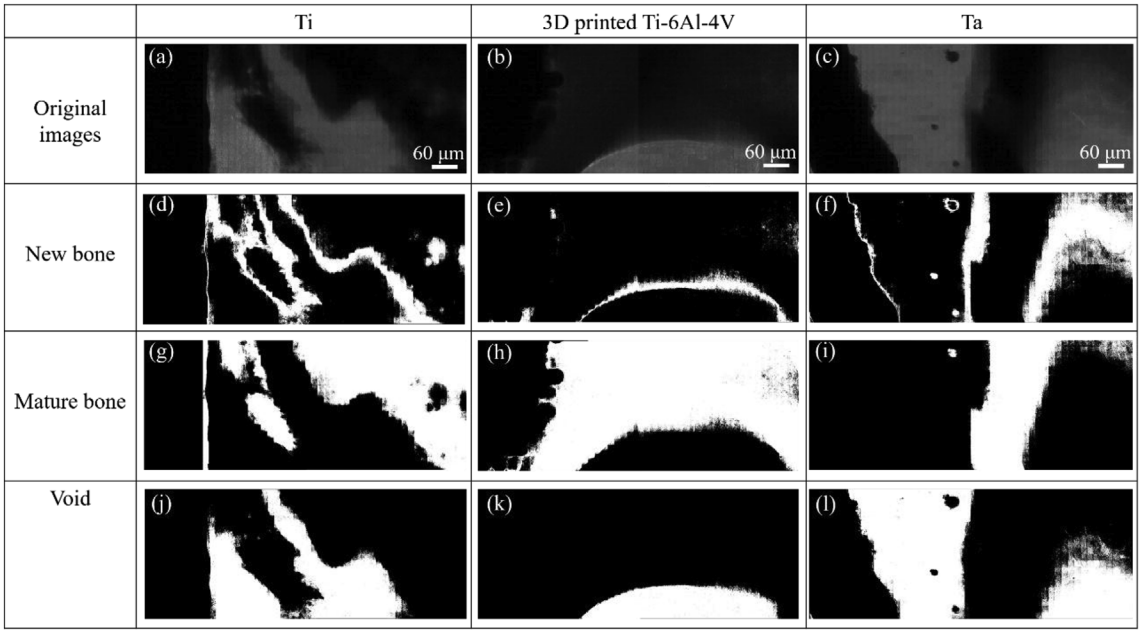

Figure 3. 2D TXM images of surrounding bone tissue growth around osteointegrated implants of (a) commercially non-porous Ti, (b) 3D printed porous Ti−6Al−4V, and (c) commercially porous Ta at the same scale bar of 60 μm. The white regions of new bone, mature bone, and void of Ti were shown in (d), (g), and (j); those of 3D printed Ti−6Al−4V in (e), (h), and (k); and those of Ta in (f), (i), and (l); respectively.

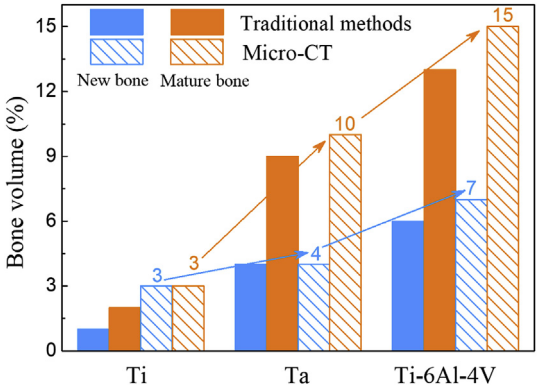

Fig. 4. Quantitative data of new bone and mature bone volume (%) calculated based on three various imaging modalities for all three different implants (Ti, Ta, and 3D printed Ti−6Al−4V). Solid blue and orange bars represent the volume of new bone determined by fluorescence and the volume of mature bone identified by RBS staining, respectively. The blue and orange patterns perform the volume percentages of new bone and mature bone detected by micro-CT, respectively. (For interpretation of the references to color in this figure legend, the reader is referred to the Web version of this article.)

and 3D printed Ti−6Al−4V implants derived by three various microscopy imaging modalities. All three of them expressed significantly higher percentages of both new bone and mature bone for porous compared to non-porous implants. Comparisons in the calculated percentages of both new bone and mature bone in each implant by micro-CT, fluorescence, and RBS staining were accordingly reported. None of the comparisons exhibited substantial variations in the percentages of new born and mature bone by those three imaging techniques, asserting the highly reliable role of micro-CT in the assessment of bone ingrowth in fusion cages. Among the three implants, the designed Ti−6Al−4V displayed the most rapid bone ingrowth with the highest proportion of both new bone and mature bone at 7 and 15%, respectively.

3.5. Anisotropy of mineral crystals of fully mature bone in 3D printed Ti−6Al−4V

In order to comprehend about the geometrical properties of the bone structures at nanometer scale, it is of great importance to identify the texture, degree of alignment, and preferential orientation of collagen-regulated mineral crystals originated from new bone and mature bone formed around the implants. Fig. 5 describes the SAXS patterns at the same areas of new bone and mature bone observed in micro-CT for all the three implants. As we can observe in Fig. 5(a) and (b), and (c), the newly formed bone around three implants displayed uniform circular SAXS patterns, which implied the random distribution and isotropy of the constituent mineral crystals. The randomly oriented crystals were also found in the mature bone of Ti implant in Fig. 5 (d) whereas the mineral crystals came from the mature bone of Ta implant in Fig. 5 (e) were slightly aligned. Otherwise, a non-circular scattering pattern in Fig. 5 (f) shows a more pronounced arrangement along a certain direction, meaning the orientation anisotropy of constituent mineral crystals of the fully mineralized mature bone around Ti−6Al−4V implant. This non-circular pattern is quite similar to SAXS pattern of the autologous bone in which a clearly predominant alignment of constituent mineral crystals was detected in Fig. S1 (supplementary information). Many factors such as bone type and the age of animal possibly govern the discrepancies observed in shape and favorable alignment of mineral crystals [52]. The dominant alignment with an angular distribution of mineral crystals in mature bone of an adult animal was proved [53,54]. It can be proposed that there is a strong correlation between the maturity degree of bone regeneration and the favorable arrangement of constituent mineral crystals. Our SAXS results imply a stronger degree of collagen-regulated mineralization in fully mature bone in the pig implanted with Ti−6Al−4V than in the one implanted with the commercially non-porous Ti and porous Ta fusion cages. This may provide positive influence on higher force required for removal of implants in extending better implant longevity.

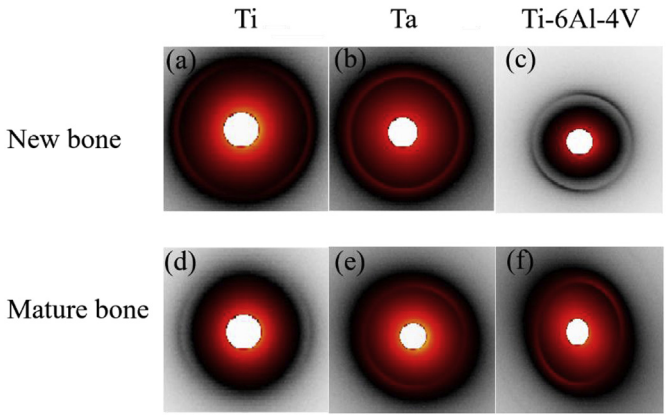

Fig. 5. SAXS patterns of mineral crystals derived from commercially non-porous Ti, porous Ta, and 3D printed Ti−6Al−4V implants collected at new bone in (a), (b), and (c), respectively, and those taken at mature bone regions in (d), (e), and (f), respectively.

3.6. Better crystalline phase of HA minerals from fully mature bone in 3D printed Ti−6Al−4V

To clarify the crystallographic structures of HA minerals originated from new bone and mature bone surrounding the three various implants, high resolution synchrotron XRD measurements were acquired. Fig. 6 presents the XRD patterns recorded from the new bone and mature bone of the three implants. In Fig. 6 (a), all the XRD patterns exhibited remarkable diffraction peaks located at (211) and (002), indicating the presence of hexagonal crystal structures of HA minerals derived from new bone and mature bone around the three implants. The highest intensities of all diffraction peaks in the fully mineralized mature bone of Ti−6Al−4V denoted a well-crystalline phase of composed HA. To make a comparison in evaluating the degree of crystallinity, the differences were obtained by subtracting the XRD profile of new bone from that of mature bone for each kind of implant, as described in Fig. 6(b). The mineral crystals from the mature bone revealed better crystallinity volumes than those from the new bone around porous Ta and Ti−6Al−4V implants whereas no noticeable difference was detected in non-porous Ti implant. It is essential to emphasize that the HA minerals from the fully mineralized mature bone in Ti−6Al−4V appeared in a better crystalline phase compared to those from the mature bone in the commercial Ti and Ta implants. Therefore, the XRD results mentioned that the more maturity the bone is, the more crystalline the constituent HA is.

3.7. The evolution of bone formation and remodeling in 3D printed Ti−6Al−4V implant

Based on the crystal structure, crystal orientation, and crystal deformation of the constituent HA minerals, we exploited nano X-ray Laue diffraction mapping to examine the evolution of bone formation and remodeling at a localized bone growth region in 3D printed Ti−6Al−4V implant. A specific bone area marked by a solid red oval in RBS staining image in Fig. 7(a) and TXM image in Fig. 7(b) was chosen to be mapped by scanning X-ray Laue diffraction. The 3D printed Ti−6Al−4V specimen was mounted on the x-y scanning stage and the expected scanning area in Fig. 7(a) and (b) was positioned by an on-axis scanning electron microscopy (SEM) in Fig. 7(c). The zero position in x-axis was

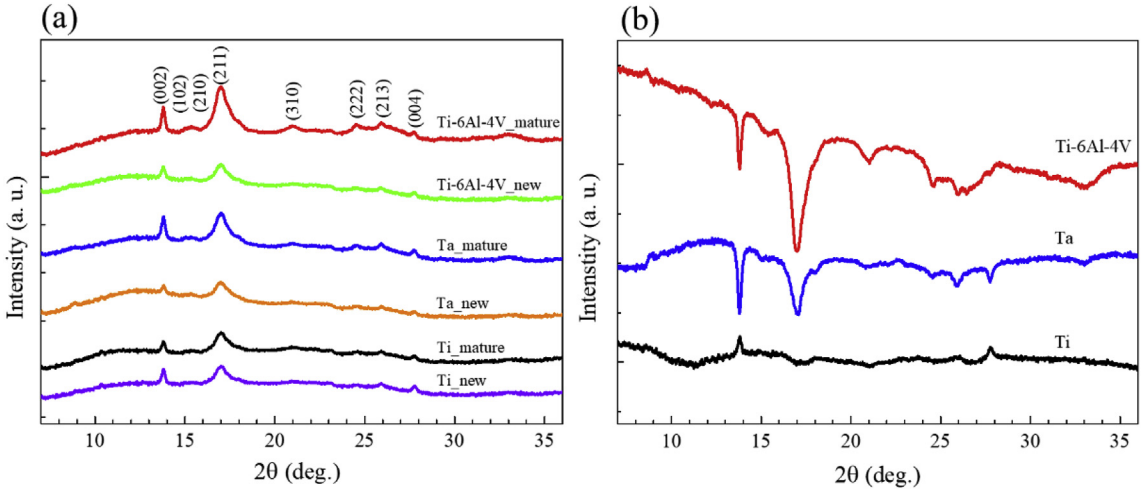

Fig. 6. (a) XRD profiles of constituent HA mineral crystals of new bone and mature bone in commercially non-porous Ti, porous Ta, and 3D printed Ti−6Al−4V implants. (b) The differences between XRD profile of new bone and that of mature bone in each type of implant.

regarded as the boundary between the void and bone growth area. The pixels in Fig. 7(d) performed the total sum intensity of diffraction spots and fluorescence background in each Laue pattern in which the brighter red color the higher density of bone formation was. The majority of pixels with identical color enclosed by the dotted black curve in Fig. 7(e) represent each individual bone region which has the same crystal orientation in a local grain. However, there are some pixels with slightly different color inside the grain, ascribed to the crystal distortion or deformation within individual bone growth regions, which is further analyzed by full width mapping of the main diffraction peak in Fig. 7(f). The higher intensity corresponds to the broader main peak, which is related to the degree of deformation or physical dimensions. We employed X-ray micro-diffraction analysis software (XMAS) developed by Dr. Nobumichi Tamura from Advanced Light Source (ALS) to index the Laue patterns for identifying the crystal structure and crystal deformation in individual bone regions, thus, the Laue diffraction patterns were extracted in Fig. 7(g) along the direction marked as the dotted magenta line in Fig. 7(d). The fitting results demonstrated the HA crystal structure of space group P63/m with the refined lattice parameters a = b = 0.944 nm and c = 0.681 nm, shown in Fig. S2 (supplementary information). The diffraction spots in the area from the boundary to position 5 μm were isotropic broadening, associated to the newly formed bone. Those diffraction spots were gradually shrank in the zone from the position 5 μm–45 μm implied the appearance of the fully mature bone. The heterogeneous broadening and elongation along a certain direction of the diffraction spots inferred high density of dislocations and residual stress in the bone resorption region from the position 45 μm–300 μm. Very sharp diffraction spots from the position 300 μm–360 μm suggested the autologous bone region.

4. Discussion

The developing status of the surrounding bone tissue around the three different types of implants was carefully assessed by three alternative examinations, of which histological staining has been known as the gold standard. Nevertheless, this method required the preparation of cage samples stained in acidified acid fuchsin and it only allowed for a clear observation of mature bone. In contrast to RBS staining, the introduction of tetracycline-based fluorochrome into the pig was necessary for the visualization of newly formed bone in fluorescence method. The other prospect approaches for a more pronounced differentiation of both new bone and mature bone are X-ray micro-CT and TXM in which no preliminary preparation of cage samples was imperative.

From the viewpoint of bone remodeling in bone healing, spinal fusion involves an intricate biomechanical process of bone regeneration so that the bone could perfectly recover to the originally normal condition [55]. Relevant stress need to be applied on bone since it is a living substance. After supporting mechanical stabilization, the initially new bone composed of organic collagen matrix starts being produced whose mineralization is in association with the evolution of HA crystallites over time, hence gradually enhances the strength of bone. The newly formed bone is sequentially substituted by mature bone whose matrix is more mineralized than new bone and is mainly responsible for capable of enduring high load. A larger volume of highly mineralized mature bone would be expected in attaining sufficient strength until full maturity of bone is reached [56]. Therefore, it can be emphasized that the greater volumes of new bone and mature bone ingrowth into the porous networks of 3D printed Ti−6Al−4V intensify interfacial strengths at the bone-implant contact when they mineralize, that effectively accelerates spinal fusion recovery process. With satisfactory results on our additive manufactured Ti−6Al−4V, exploring new potentially promising metallic biomaterials for efficiently promoting bone growth and osseointegration is full of promise.

The success of implants is not only related to osseointegration but also the bone remodeling around the implants [56]. The morphological and biochemical alterations associated with the bone remodeling process occur around the implants from 1 to 3.5 months after osseointegration. The rapid growth of bone remodeling status in bone healing around the implants is very salient for the determination of implant stability and survival especially for dental screws or spinal fusion cages [57,58]. Current bone healing detection methods such as radiography or computed tomography are hard to provide detail information about bone maturity and implant pore bone-ingrowth [59]. Some other methods had been proposed such as histology, time-of-flight secondary ion mass spectrometry (TOF-SIMS) in vitro models may provide good details but might be associated with technical difficulties such as staining conditions. Fluorescence microscopy techniques had been developed as a healing evaluation tool in vivo models but will need to give fluorescence cell into living animals [60]. The limitation of these methods is the need to have special staining or medication which might not be applicable in clinical settings. Our study utilizes X-ray micro-CT, TXM, SAXS, and XRD to evaluate the bone healing process around the implants and confirms the better design of additive manufactured Ti−6Al−4V cage compared to non-porous Ti and porous Ta cages. These detection methods might pave an auspicious way for future directions in clinical applications.

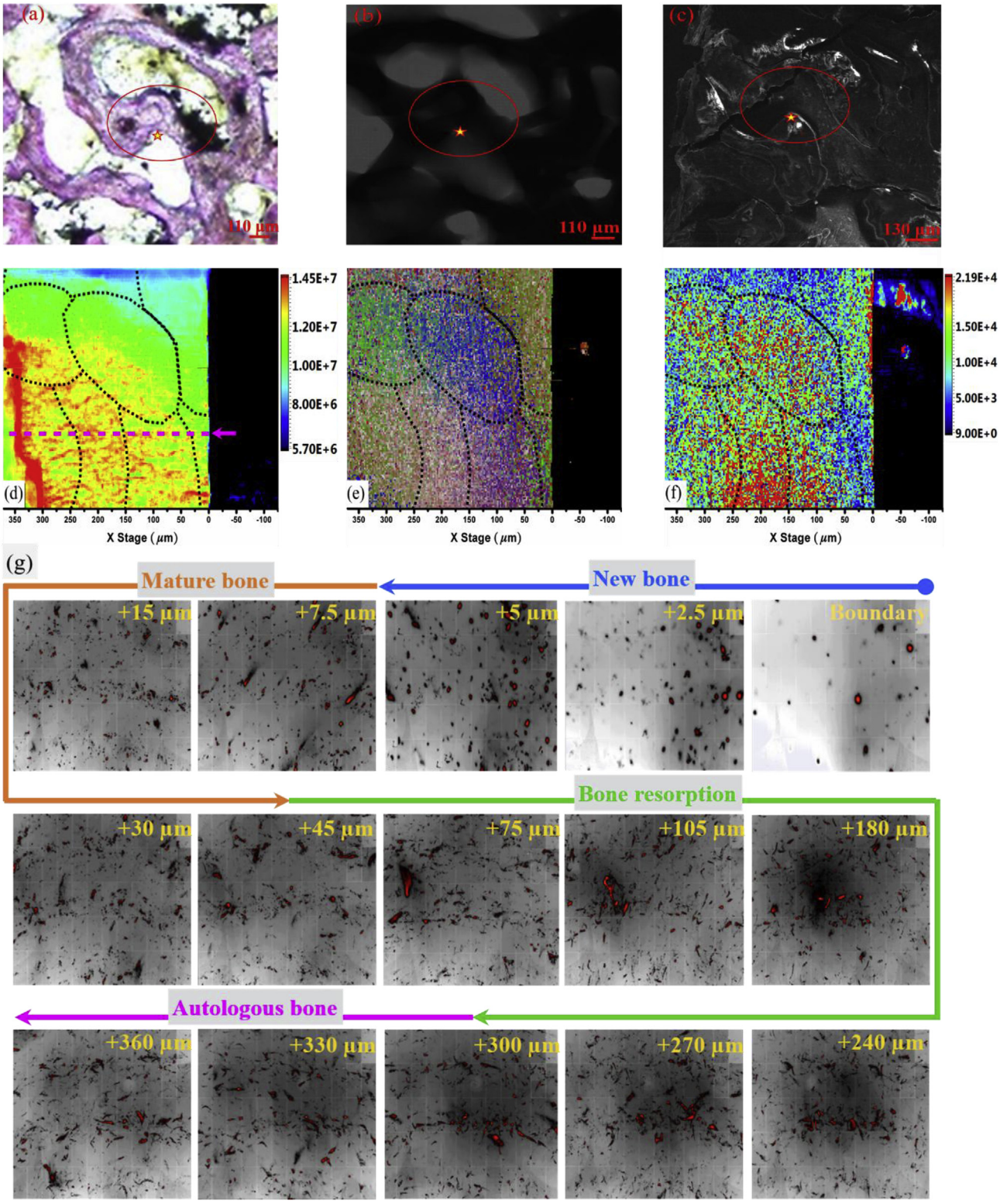

Fig. 7. A localized bone area in porous Ti−6Al−4V specimen marked by the solid red oval in (a) RBS staining, (b) TXM, and (c) SEM image. The star symbol used for positioning. Three distinct microstructural maps of scanning X-ray Laue diffraction: (d) total intensity map from diffraction patterns, (e) crystal orientation map, and (f) full width map of main diffraction peak. (g) The Laue diffraction patterns extracted from the direction marked as the dotted magenta line. (For interpretation of the references to color in this figure legend, the reader is referred to the Web version of this article.)

5. Conclusions

The microstructural imaging modalities demonstrated that animals implanted with additive manufactured Ti−6Al−4V cages had significantly more pronounced volumes of new bone and mature bone tissue adaption around periphery and stronger surface osseointegration compared to those implanted with the commercial Ti and Ta cages. The isotropic distribution of mineral crystals from newly formed bone was

identified for all the three implants. The predominant alignment of HA crystallites derived from the mature bone of 3D printed Ti−6Al−4V proposed the enhancement of the collagen-regulated mineralization in fully mineralized mature bone which also revealed higher crystallinity volumes compared to those of Ti and Ta implants. The microstructural and nanostructural properties allude the high quality of bone formed around the designed Ti−6Al−4V rather than around the commercial Ti and Ta cages. The well-designed Ti−6Al−4V alloy fabricated by SLM provides a priority candidate for facilitating bony healing process of next generation use in spinal fusion cages.

Author contributions

Pei-I Tsai and Tu-Ngoc Lam contributed equally to this work. EWH outlined and supervised the research. CCW performed and analyzed X-ray micro-CT and TXM. PIT performed and analyzed staining and fluorescence analysis. TNL prepared the manuscript. MHW, JSS, YYL, and MHL performed in vivo study and analyzed clinical information. KYT and YWC performed, collected, and analyzed the data for synchrotron-based experiments. CHL, CYC, and CSK helped to perform and analyze nano X-ray diffraction. NTT, SJS, and SYC commented on the manuscript. CKC helped to perform synchrotron XRD. CJS helped to perform and analyze SAXS. All authors revised the manuscript and approved the final version.

Conflicts of interest

The authors declare no competing financial interest.

Acknowledgements

EWH appreciates the support from Ministry of Science and Technology Programs 104-2628-E-009-003-MY3, 106-2811-E-009-032, 106-2218-E-007-019, 106-2514-S-007-004, and 106-3011-F-002-002, 107-3017-F-009-002, 107-3011-F-002-002, 107-2628-E-009-001-MY3, and 107-2218-E-009-003. We thank the ITRI Programs F301AR7Z50, G301AR7Z50, and GM5400J000TNL. Meng-Huang Wu and Yen-Yao Li were supported by the Chang Gung Memorial Hospital (CMRPG6D0171-172). Pei-I Tsai was supported by ITRI Program F301AR5F20. Tu-Ngoc Lam was supported by MOST107-2628-E-009-001-MY3 and “Center for Semiconductor Technology Research” 107W302 from The Featured Areas Research Center Program within the framework of the Higher Education Sprout Project by the Ministry of Education (MOE) in Taiwan. We greatly appreciate Dr. Yeu-Kuang Hwu at the Institute of Physics, Academia Sinica for the help of the X-ray micro-CT data collection, and the beam time and help from the National Synchrotron Radiation Research Center (NSRRC). The authors specially thank Ms. Shin-Yi Huang from the Industrial Technology Research Institute (ITRI) for preparation of bone samples.

Appendix A. Supplementary data

Supplementary data to this article can be found online at https://doi.org/10.1016/j.matchemphys.2019.03.047.

References

[1] A.R.N. Fereshteh A. Sabet, Elham Hamed, Iwona Jasiuk, Modelling of bone fracture and strength at different length scales: a review, Interface Focus 6 (2016) 20150055.
[2] V.A.S. Claire Acevedo, Dominique P. Pioletti, Tamara Alliston, Robert O. Ritchie, Fatigue as the missing link between bone fragility and fracture, Nat. Biomed. Eng. 2 (2018) 62–71.
[3] F. Rauch, Bone growth in length and width: the Yin and Yang of bone stability, J. Musculoskelet. Neuronal Interact. 5 (2005) 194–201.
[4] E.G. Suwimon Boonrungsiman, Raffaella Carzaniga, Nicholas D. Evans, David W. McComb, Alexandra E. Porter, Molly M. Stevens, The role of intracellular calcium phosphate in osteoblast-mediated bone apatite formation, Proc. Natl. Acad. Sci. Unit. States Am. 109 (2012) 14170–14175.
[5] G.G. Ignac Fogelman, Hans Van der Wall, Radionuclide and Hybrid Bone Imaging, Springer-Verlag Berlin Heidelberg, 2012, p. 29.
[6] A.G.a.A. Veis, Phosphorylated proteins and control over apatite nucleation, crystal growth, and inhibition, Chem. Rev. 108 (2008) 4670–4693.
[7] A.V.a.J.R. Dorvee, Biomineralization mechanisms: a new paradigm for crystal nucleation in organic matrices, Calcif. Tissue Int. 93 (4) (2013) 307–315.
[8] J.-H.J. Kyung Mi Woo, Victor J. Chen, Jihye Seo, Jeong-Hwa Baek, Hyun-Mo Ryoo, Gwan-Shik Kim, Martha J. Somerman, Peter X. Ma, Nano-fibrous scaffolding promotes osteoblast differentiation and biomineralization, Biomaterials 28 (2007) 353-343.
[9] C.Y. Lin, T. Wirtz, F. LaMarca, S.J. Hollister, Structural and mechanical evaluations of a topology optimized titanium interbody fusion cage fabricated by selective laser melting process, J. Biomed. Mater. Res. A 83 (2007) 272–279.
[10] B.O.H.P.I. Branemark, R. Adell, U. Breine, J. Lindström, O. Hallen, A. Ohman Osseointegrated im- plants in the treatment of the edentulous jaw. Experience from a 10-year period, Scand. J. Plast. Reconstr. Surg. Suppl. 16 (1977) 1–132.
[11] B. GW, Arthrodesis by the distraction-compression method using a stainless steel implant, Orthopedics 11 (1988) 931–934.
[12] S.A. Brantigan JW, J.M. Geiger, A carbon fiber implant to aid interbody lumbar fusion: mechanical testing, Spine 16 (1991) 277–282.
[13] R. CD, Threaded titanium cages for lumbar spine, Spine 22 (1997) 667–679.
[14] E.D. Herderick, Additive manufacturing in the minerals, metals, and materials community: past, present, and exciting future, JOM (J. Occup. Med.) 68 (2016) 721–723.
[15] S.K. Sinclair, G.J. Konz, J.M. Dawson, R.T. Epperson, R.D. Bloebaum, Host bone response to polyetheretherketone versus porous tantalum implants for cervical spinal fusion in a goat model, Spine (Phila Pa 37 (2012) E571–E580 1976.
[16] T.H.S. Martijn van Dijk, Elisabeth H. Burger, Paul I. Wuisman, Bioabsorbable poly-L-lactic acid cages for lumbar, Spine 27 (2002) 2706–2714.
[17] K. Alvarez, H. Nakajima, Metallic scaffolds for bone regeneration, Materials 2 (2009) 790–832.
[18] E.v.d.Z. A. Schroeder, H. Stich, F. Sutter, The reaction of bone, connective tissue and epithelium to endosteal implants with sprayed titanium surfaces, I. Max. Fac. Surg. 9 (1981) 15–25.
[19] G.H. Hille, Titanium for surgical implants, J. Mater. 1 (1966) 373–381.
[20] T. Albrektsson, P.I. Brånemark, H.A. Hansson, J. Lindström, Osseointegrated titanium implants:requirements for ensuring a long-lasting, direct bone-to-implant anchorage in man, Acta Orthop. Scand. 52 (1981) 155–170.
[21] R.M.P.-s. Pilliar, Porous-surfaced metallic implants for orthopedic applications, J. Biomed. Mater. Res. 21 (1987) 1–33.
[22] D.P. Collier, M.B. Mayor, J.C. Chae, Macroscopic and microscopic evidence of prosthetic fixation with porous-coated materials, Clin. Orthop. Relat. Res. 3 (1998) 249–262.
[23] B.J. Sajad Arabnejad, Michael Tanzer, Damiano Pasini, Fully porous 3D printed titanium femoral stem to reduce stress-shielding following total hip arthroplasty, J. Orthop. Res. 35 (2017) 1774–1783.
[24] E.M. Luca Facchini, Pierfrancesco Robotti, Alberto Molinari, Hoges Simon, Konrad Wissenbach, Ductility of a Ti-6Al-4V alloy produced by selective laser melting of prealloyed powders, Rapid Prototyp. J. 16 (2010) 450–459.
[25] A.A. Zadpoor, Bone tissue regeneration: the role of scaffold geometry, Biomater. Sci. 3 (2015) 231–245.
[26] E.B.a.S.B. Bhaduri, Fabrication aspects of porous biomaterials in orthopedic applications: a review, ACS Biomater. Sci. Eng. 4 (2018) 1–39.
[27] X. Liu, S. Chen, J.K.H. Tsoi, J.P. Matinlinna, Binary titanium alloys as dental implant materials-a review, Regen Biomater 4 (2017) 315–323.
[28] F.A. Shah, A. Snis, A. Matic, P. Thomsen, A. Palmquist, 3D printed Ti6Al4V implant surface promotes bone maturation and retains a higher density of less aged osteocytes at the bone-implant interface, Acta Biomater. 30 (2016) 357–367.
[29] X. Zhang, G. Zheng, J. Wang, Y. Zhang, G. Zhang, Z. Li, Y. Wang, Porous Ti6Al4V scaffold directly fabricated by sintering: preparation and in vivo experiment, J. Nanomater. 2013 (2013) 1–7.
[30] P.J. Withers, M. Preuss, Fatigue and damage in structural materials studied by X-ray tomography, Annu. Rev. Mater. Res. 42 (2012) 81–103.
[31] C.W. Levi AD, P.J. Keller, J.E. Heiserman, V.K. Sonntag, C.A. Dickman, The radiographic and imaging characteristics of porous tantalum implants within the human cervical spine, Spine 23 (1998) 1245–1251.
[32] Y.W. Wang JC, H.S. Sandhu, V. Tam, R.B. Delamarter, A comparison of magnetic resonance and computed tomographic image quality after the implantation of tantalum and titanium spinal instrumentation, Spine 23 (1998) 1684–1688.
[33] B.J, Biological performance of tantalum, Clin. Mater. 16 (1994) 167–173.
[34] H.W.B. Ben B. Pradhan, Edgar G. Dawson, Vikas V. Patel, Rick B. Delamarter, Graft resorption with the use of bone morphogenetic, Spine 31 (2006) E277–E284.
[35] S. Tadano, B. Giri, X-ray diffraction as a promising tool to characterize bone nanocomposites, Sci. Technol. Adv. Mater. 12 (2011) 064708.
[36] S.P. Karen, J.L. Burg, James F. Kellam, Biomaterial developments for bone tissue engineering, Biomaterials 21 (2000) 2347–2359.
[37] F. Yang, C. Chen, Q. Zhou, Y. Gong, R. Li, C. Li, F. Klampfl, S. Freund, X. Wu, Y. Sun, X. Li, M. Schmidt, D. Ma, Y. Yu, Laser beam melting 3D printing of Ti6Al4V based porous structured dental implants: fabrication, biocompatibility analysis and photoelastic study, Sci. Rep. 7 (2017) 45360.
[38] C.K.C.C.Y. Yap, Z.L. Dong, Z.H. Liu, D.Q. Zhang, L.E. Loh, S.L. Sing, Review of selective laser melting: materials and applications, Appl. Phys. Rev. 2 (2015) 041101.
[39] J. Banks, Adding value in additive manufacturing: researchers in the United Kingdom and Europe look to 3D printing for customization, IEEE Pulse 4 (2013)

22–26.
[40] D.Z. Yangli Xu, Yan Zhou, Weidong Wang, Xuanyang Cao, Study on topology optimization design, manufacturability, and performance evaluation of Ti-6Al-4V porous structures fabricated by selective laser melting (SLM), Materials 10 (2017) 1048.
[41] B.R. Sanderson C, Advances in the staining of ground section histology, Hisro-Logic XXIII (1993) 1–3.
[42] C. Pautke, S. Vogt, K. Kreutzer, C. Haczek, G. Wexel, A. Kolk, A.B. Imhoff, H. Zitzelsberger, S. Milz, T. Tischer, Characterization of eight different tetracyclines: advances in fluorescence bone labeling, J. Anat. 217 (2010) 76–82.
[43] C.W. Chaohua Gao, Hui Jin, Zhonghan Wang, Zuhao Li, Chenyu Shi, Leng Yi, Yang Fan, Liu He, Jincheng Wang, Additive manufacturing technique-designed metallic porous implants for clinical application in orthopedics, RSC Adv. 8 (2018) 25210–25227.
[44] J.M. Murat Guvendiren, Rosane M.D. Soares, Joachim Kohn, Designing biomaterials for 3D printing, ACS Biomater. Sci. Eng. 2 (2016) 1679–1693.
[45] D.W.H.a.M.M. Thornton, Micro-CT in small animal and specimen imaging, Trends Biotechnol. 20 (2002) S34–S39.
[46] S.R. Stock, D. Blackburn, M. Gradassi, H.G. Simon, Bone formation during forelimb regeneration: a microtomography (microCT) analysis, Dev. Dynam. 226 (2003) 410–417.
[47] Y.-F.S. Chun-Chieh Wang, Sheng-Rong Song, Qiang Ji, Cheng-Cheng Chiang, Qingjin Meng, Haibing Li, Kiko Hsiao, Yi-Chia Lu, Bor-Yuan Shew, Timothy Huang, Robert R. Reisz, Evolution and function of dinosaur teeth at ultramicrostructural level revealed using synchrotron transmission X-ray microscopy, Sci. Rep. 5 (2015) 1–11.
[48] W.-J.H. Tu-Ngoc Lam, Chun-Chieh Wang, Wei-Tsung Chuang, Ya-Wen Su, E-Wen Huang, Micro-layer and lattice structure effects on impedance of titanium oxide phthalocyanine, Adv. Eng. Mater. 1701140 (2018) 1–5.
[49] P. Fratzl, S. Schreiber, K. Klaushofer, Bone mineralization as studied by small-angle x-ray scattering, Connect. Tissue Res. 34 (1996) 247–254.
[50] M.C.D. Carlo Meneghini, Stefania Nuzzo, Settimio Mobilio, Rudy H. Wenk, Rietveld refinement on x-ray diffraction patterns of bioapatite in human fetal bones, Biophys. J. 84 (2003) 2021–2029.
[51] R.B.a.G. Ice, Strain and Dislocation Gradients from Diffraction, Imperical College Press, 2014, pp. 125–155.
[52] S.H. Quan Liu, Jukka Pekka Matinlinna, Zhuofan Chen, Haobo Pan, Insight into biological apatite: physiochemical properties and preparation approaches, BioMed Res. Int. (2013) 1–13 2013.
[53] N.F.-Z. Peter Fratzl, Klaus Klaushofer, Gero Vogl, Kristian Koller, Nucleation and growth of mineral crystals in bone studied by small-angle X-ray scattering, Calcif. Tissue Int. 48 (1991) 407–413.
[54] A.M. Matsushima N, Y. Terayama, Quantitative analysis of the orientation of mineral in bone from small angle x-ray scattering patterns, Jpn. J. Appl. Phys. 21 (1982) 186–189.
[55] P.J.P.D. Lacroix, G. Li, D. Marsh, Biomechanical model to simulate tissue differentiation and bone regeneration Application to fracture healing, Med. Biol. Eng. Comput. 40 (2002) 14–21.
[56] L.S.P. Diane, M. Robert, Ramlal Chahal, Preliminary observations of bone ingrowth into porous materials, J. Biomed. Mater. Res. 10 (1976) 335–344.
[57] M.B. Rodolfo, B. Anchieta, Fernando Guastaldi, Nick Tovar, Malvin N. Janal, Gottlow Jan, Michel Dard, Ryo Jimbo, Paulo G. Coelho, Mechanical property assessment of bone healing around a titanium–zirconium alloy dental implant, Clin. Implant Dent. Relat. Res. 16 (2014) 913–919.
[58] H.C. Lee, P.I. Tsai, C.C. Huang, S.Y. Chen, C.G. Chao, N.T. Tsou, Numerical method for the design of healing chamber in additive-manufactured dental implants, BioMed Res. Int. 2017 (2017) 1970680.
[59] P.G. Shikha Nandal, Himanshu Shekhawat, A radiological evaluation of marginal bone around dental implants: an in-vivo study, Natl. J. Maxillofac. Surg. 5 (2014) 126–137.
[60] M.B. Cecilia Eriksson, Håkan Nygren, Lars O ¨ ster, Novel in vivo method for evaluation of healing around implants in bone, J. Biomed. Mater. Res. A 66 (2003) 662–668.